

Research Article

Higher-Order Mode Electromagnetic Analysis of a Material Sample between Two Flanged Coaxial Probes for Broadband Modelling of Dielectric Measurement Setups

Raúl V. Haro-Báez,^{1,2} Juan Córcoles ,² Jorge A. Ruiz-Cruz ,² José R. Montejo-Garai,³ and Jesús M. Rebollar³

¹Universidad de las Fuerzas Armadas ESPE, Departamento de Eléctrica y Electrónica, Quito 171103, Ecuador

²Universidad Autónoma de Madrid, Escuela Politécnica Superior, C/Francisco Tomás y Valiente 11, Madrid 28049, Spain

³Universidad Politécnica de Madrid, Departamento de Señales, Sistemas y Radiocomunicaciones, Ciudad Universitaria s/n, Madrid 20840, Spain

Correspondence should be addressed to Juan Córcoles; juan.corcoles@uam.es

Received 5 November 2018; Accepted 25 December 2018; Published 10 January 2019

Academic Editor: John D. Clayton

Copyright © 2019 Raúl V. Haro-Báez et al. This is an open access article distributed under the Creative Commons Attribution License, which permits unrestricted use, distribution, and reproduction in any medium, provided the original work is properly cited.

The characterization of the dielectric properties of a material requires a measurement technique and its associated analysis method. In this work, the configuration involving two coaxial probes with a material for dielectric measurement between them is analyzed with a mode-matching approach. To that effect, two models with different complexity and particularities are proposed. It will be shown how convergence is sped up for accurate results by using a proper choice of higher-order modes along with a combination of perfect electric wall and perfect magnetic wall boundary conditions. It will also be shown how the frequency response is affected by the flange mounting size, which can be, rigorously and efficiently, taken into account with the same type of approach. This numerical study is validated through a wide range of simulations with reference values from another method, showing how the proposed approaches can be used for the broadband characterization of this well-known, but with a recent renewed interest from the research community, dielectric measurement setup.

1. Introduction

The behavior of a material under the exposure to electromagnetic fields is determined by its dielectric properties. The accurate knowledge of these properties is essential in science and engineering, since they are used in a variety of industries [1, 2]. The properties of a material can be tracked during an industrial process, and, thus, they can be used to monitor a product, incorporating that information into an improved quality control. They are also important in diverse fields such as remote sensing, heating, molecular analysis, and creation of liquid standards [3, 4].

More specifically, in microwave engineering [5, 6], the dielectric properties of materials are key data for evaluating the performance of circuit substrates, printed antennas, radomes, dielectric resonators, etc. [7]. In modern computer

aided design, these properties are incorporated in the so-called full-wave methods (techniques to solve the Maxwell equations starting from the full electromagnetic model) in order to provide accurate predictions for each application. In the telecommunications industry, with a massive use of the microwave spectrum, the precise characterization of the materials involved in the microwave components is essential to optimize and make designs with stringent electrical specifications, which are becoming progressively more demanding to address new systems with higher data capacity.

Regardless of the specific area where the dielectric properties are required, the process to characterize them is based on two techniques: (i) a measurement technique extracting a parameter related directly or (more commonly) indirectly with the dielectric properties and (ii) an electromagnetic analysis technique (circuit-based or full-wave) modelling the

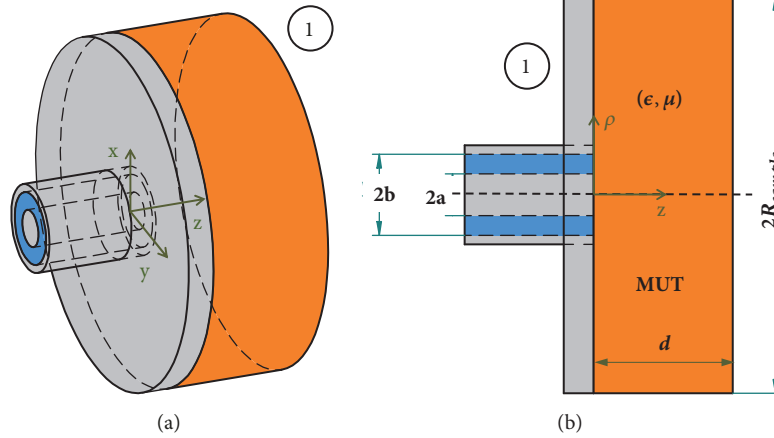


FIGURE 1: Schematic of the one-port open coaxial used for dielectric measurement, showing the material under test (MUT) with its dielectric properties: (a) 3D schematic view; (b) longitudinal cut (revolution symmetry with respect to z).

measurement, i.e., providing estimations of the results of that measurement for a given material.

With respect to the measurement techniques, there is a plurality of options, such as those based on coaxial probes, transmission lines, free space methods, use of resonators (as in microwave filter characterization), etc. [1]. This variety of measurement techniques provides different alternatives for dealing with constrains in the frequency range, the requirements of preparation for the sample, type of expected (low/high) losses in the material, etc. In this work, the coaxial probe will be used, since it provides a good trade-off between many of these features, can be used for biological tissues, and can be considered a broadband method, which is one of the goals of this paper. In addition, its use is very simple and well-known, especially in microwave engineering, where it has been used for a long time [8–11].

With respect to the analysis technique used in the dielectric characterization process, when the electromagnetic analysis is based on a full-wave approach, the results will be more precise, at the expense of a higher computational burden than simpler circuit analyses. This paper will use an accurate full-wave electromagnetic method based on mode-matching methods [12, 13], which provide more accurate estimations than circuital methods. In comparison with other full-wave methods [14], it also shows a great efficiency, which will be further improved by exploiting the specific features of the geometry associated with the two-port coaxial probe measurement problem.

In fact, this kind of problem has received very recent attention for different types of materials and with different types of probes for the input/output [15–17]. In this paper, two different models based on mode-matching along the longitudinal direction are proposed for characterizing the two-port problem associated with the coaxial probe for dielectric measurement of homogeneous samples. The first model will benefit from different types of boundary conditions that can be used to model the simplest structure, made up of two coaxial lines with the material to be measured inserted in a virtual circular waveguide that contains the

sample. This circular waveguide will be modelled with perfect electric or magnetic wall boundary conditions and with a combination of both cases, which will be shown to provide faster convergent results. The second model will also take the flanges of the setup into account. The convergence of these models with respect to different parameters will be studied, resulting in a very efficient tool that can be used for the broadband analysis of the two-port scattering problem of a material sample placed between two coaxial probes for dielectric measurement.

2. The Coaxial Probe for Dielectric Measurement

2.1. One-Port Open Coaxial Probe. The coaxial probe open at one end, whose basic schematic version is shown in Figure 1, is one of the preferred techniques for measuring materials. It is a very simple setup, where the sample material can be inserted in the test unit with almost no preparation, filling the space just after the coaxial probe. This can be easily done for a large variety of malleable materials such as liquids or semisolids whose shape can be adjusted. However, for solids, contact surfaces must be flat enough and tighten to the test unit in order to avoid air gaps between the sample and the probe that will degrade the measurement.

From the electromagnetic point of view, the problem in Figure 1 is a coaxial probe radiating in a semi-infinite space (the orange block in the figure) whose dielectric properties are those of the material under test (MUT), which may have losses: complex dielectric permittivity $\epsilon = \epsilon' - j\epsilon''$ and complex magnetic permeability $\mu = \mu' - j\mu''$. The coaxial transmission line has two conductors of internal and external radius a and b , respectively, with a supporting dielectric (blue color in Figure 1). These parameters are typically adjusted for providing 50Ω characteristic impedance, as in classic microwave equipment. In the analysis technique, a semi-infinite space is assumed for the region related to the MUT, and, thus, the thickness (d) and the transversal size of the sample (R_{sample}) must be electrically large enough in order

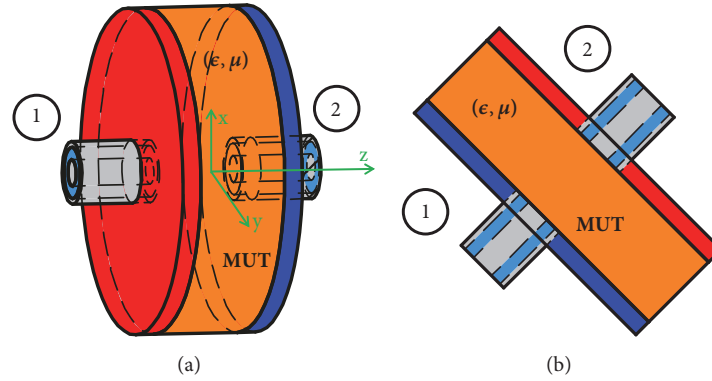


FIGURE 2: Schematic of the two-port coaxial holder for dielectric measurement, showing the material under test (MUT): (a) 3D schematic view; (b) longitudinal cut (revolution symmetry with respect to z).

to confine the incoming electromagnetic field excited by the probe within the MUT limits. Within the same modelling, the metallic flange is assumed to be large enough for avoiding backward radiation.

The measurement technique for this case extracts the reflected electromagnetic wave at the one-port problem. The signal excited by the generator connected to the coaxial propagates through the transmission line and reaches the material, where it is partially reflected back. This reflection coefficient depends on the electromagnetic properties of the dielectric material. Thus, from this measurement, the values of the dielectric properties of the material in contact with the probe can be estimated. However, there is not a direct closed formula relating the ϵ , μ of the MUT (this is the goal of the dielectric characterization process) to the measured reflection coefficient, and this is where the different analysis techniques, from equivalent circuits to full-wave approaches, play a key role. It is important to note that this is also a classic problem in microwave engineering when designing antenna feed systems, and, thus, there has been continuous research in this subject from different perspectives during the last decades [8–11, 18–21]. These models have evolved between the complexity of the lumped and distributed elements in the initial equivalent circuits, to the way of approximating the electromagnetic field functions in the more recent full-wave approaches.

2.2. Proposed Models for the Characterization of the Two-Port Problem. The two-port measurement is a method directly related to the coaxial probe [22–24], where a thin sample of the MUT is inserted between two coaxial lines as in Figure 2, allowing a quick measurement of the return and insertion loss as a function of frequency. The analysis methods are very closely related to the coaxial probe discussed in the previous subsection. Nevertheless, different formulations have been the subject of research in very recent years [15–17].

In this work, the two models shown in Figure 3 will be proposed for MUTs with homogeneous dielectric properties. The simplest model A is shown in Figures 3(a) and 3(b). It will allow a straight analysis through mode-matching, since it involves a problem with two waveguide discontinuities

between coaxial and circular waveguides [25] surrounded by perfect electric wall (PEW) at its boundaries. A variation will be introduced to account for the particularities of the circular waveguide that contains the sample. The computations will be also done with a waveguide having perfect magnetic wall (PMW) at its boundaries and with a combination of both PEW/PMW. Their convergence properties will be tested, allowing us to decide the faster method for the two-port problem characterization.

An alternative model B is shown in Figures 3(c) and 3(d), which takes the finite flanges associated with the input/output coaxial lines into account. This model can also be simulated with mode-matching, as long as the problem of waveguide bifurcations is included in the formulation. This type of approach has been used in the past for probes and, more recently, to improve the mode-matching accuracy in radiation problems [11, 26, 27]. In this work, the model which incorporates the finite flange information will be proposed for the two-port coaxial holder. It will exploit, as model A, the advantage of the circular revolution, since only modes with no circular variation will be needed to solve this problem.

3. Electromagnetic Analysis of the Proposed Models through Mode-Matching

The proposed two models are analyzed with the mode-matching method, comprised of two main stages. First, the modes of all the waveguides involved in the problem are calculated. Then, the modal series to expand the fields in each waveguide are matched at each side of the step discontinuity, providing the Generalized Scattering Matrix (GSM) of each step. Finally, the GSMs of each step are cascaded [14, 28]. The main steps are briefly described now.

3.1. Characterization of the Waveguides. The electromagnetic field inside homogeneous waveguides can be described in terms of transversal electromagnetic (TEM), transversal electric (TE), and transversal magnetic (TM) modes [29]. The electromagnetic field of a TE or TM mode is derived from a scalar function Φ which is the solution to the

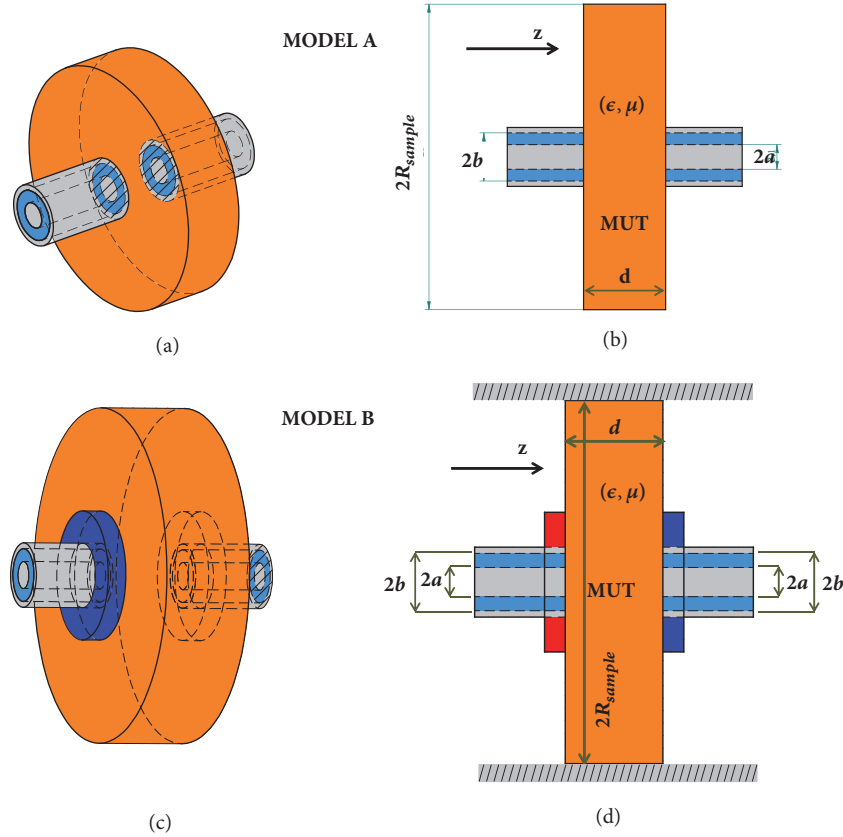


FIGURE 3: Schematic proposed models for the two-port characterization (additional details will be given in Figures 6 and 14). Model A: circular waveguide with material sample within two coaxial lines: (a) 3D view; (b) longitudinal cut with dimensions defining the problem. Model B taking the flange into account: (c) 3D view; (d) longitudinal cut with main dimensions.

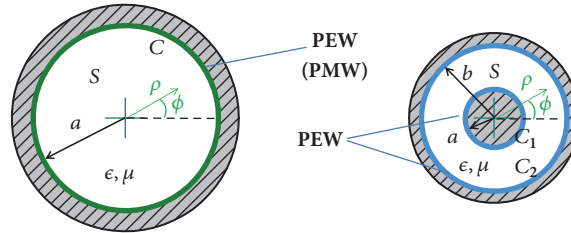


FIGURE 4: Cross-section of the type of homogenous waveguides used in this work: circular (with PEW and PMW boundary conditions) and circular coaxial.

Helmholtz equation with Neumann or Dirichlet boundary conditions:

$$\begin{aligned} \nabla_t^2 \Phi + k_c^2 \Phi &= 0, \quad \text{in } S, \quad \text{with } \nabla_t \Phi \cdot \hat{n}|_C = 0 \quad (\text{TE}), \\ \nabla_t^2 \Phi + k_c^2 \Phi &= 0, \quad \text{in } S, \quad \text{with } \Phi|_C = 0 \quad (\text{TM}), \end{aligned} \quad (1)$$

where ∇_t is the transversal to z (two dimensional) nabla differential operator, S is the cross-section with normal \hat{n} , and C is its contour. In our case for the models in Figure 3, only coaxial and circular waveguides are needed, as shown in Figure 4. In (1), function Φ is the longitudinal z -component, up to a constant factor (not depending on the spatial point), of the magnetic or electric modal field, of the TE or TM mode,

respectively. The cutoff frequency of the mode is directly related to the cutoff wavenumber of the mode k_c [7, 29].

For the coaxial waveguide, the TEM mode is also necessary to build the complete mode spectrum of the waveguide, and it can be easily computed analytically by solving the Laplace equation, where Φ represents the potential function that provides the electric field:

$$\nabla_t^2 \Phi = 0, \quad \text{in } S, \quad \text{with } \Phi|_{C_i} = v_i, \quad i = 1, 2 \quad (\text{TEM}). \quad (2)$$

Once Φ is solved for TE, TM, and TEM modes, the transversal components are obtained using basic gradient operations [7, 29]. When the cross-section of the waveguide belongs to a canonical case (such as rectangular or circular), the function Φ is readily obtained by applying the technique

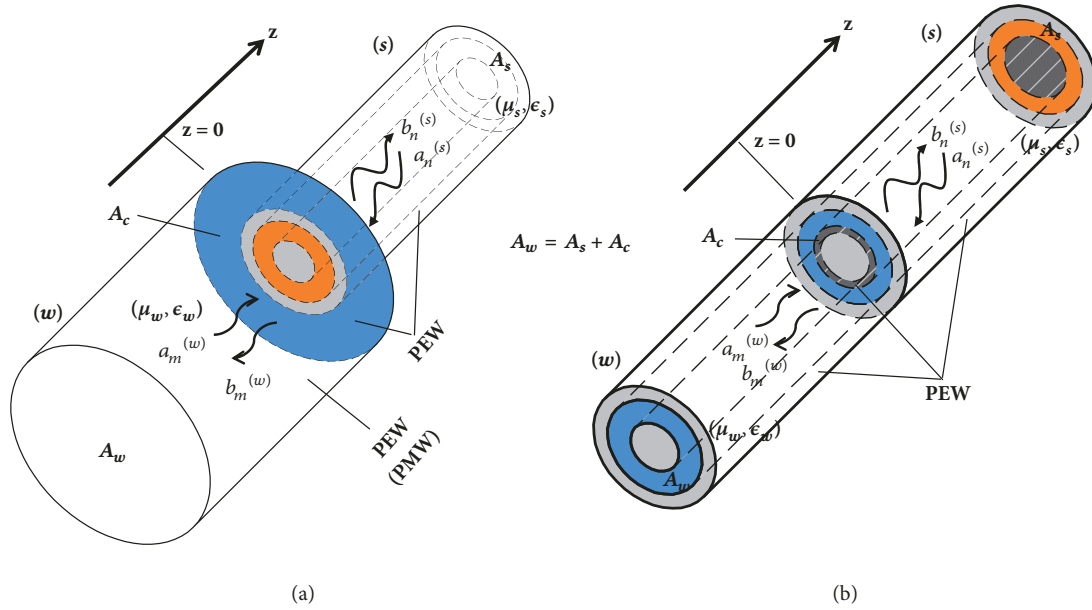


FIGURE 5: Basic waveguide step between circular and coaxial waveguides for the models in Figure 3.

of the separation of variables. In our case, it is well-known that the longitudinal field of the TE and TM modes for the waveguides in Figure 4 is written in terms of the Bessel function of the first (J_n) and second kind (Y_n):

$$\Phi = K C_n(k_c \rho) \begin{pmatrix} \cos(n\phi) \\ \sin(n\phi) \end{pmatrix}, \quad (3)$$

where K is related to the power carried by the mode and is thus used as a normalization factor. For a hollow circular waveguide, $C_n(u) = J_n(u)$ in (3). The cutoff wavenumbers of the modes for a PEW circular waveguide are $k_c^{TE} = p'_{mn}/a$, $k_c^{TM} = p_{mn}/a$, and p_{mn}, p'_{mn} are the zeros of $J_n(u)$ and $J'_n(u)$, respectively. For a PMW boundary at the circular waveguide, the dual solution with $k_c^{TE} = p_{mn}/a$, $k_c^{TM} = p'_{mn}/a$ is obtained [29]. This case for PMW is also found in [27], where the virtual waveguide with PMW is used for improving the field approximation in horn problems. For a coaxial waveguide in (3), $C_n(u) = AJ_n(u) + BY_n(u)$ is a combination of Bessel functions whose amplitudes and the cutoff wavenumber are obtained by imposing the boundary condition at the contour [7, 29].

It is important to note that the cutoff wavenumbers for the coaxial waveguide must be computed for each specific aspect ratio b/a . Nevertheless, in our problem, since the structure will be excited with a TEM mode, which does not have angular variation and has PMW symmetry at both xz - and yz -planes, all the higher-order modes generated in the structure are TM_{0n} modes in both the circular and coaxial waveguides.

3.2. Mode-Matching Formulation. As every waveguide in the two models of Figure 3 is surrounded by PEW (or PMW), the transverse electromagnetic field in these structures can be expanded in a set of orthogonal TE, TM, and TEM modes

formulated in the previous section (although TE modes will not be needed as discussed in previous section, they will be kept in this formulation for the sake of the generality). With them, the electromagnetic field in each point of the structure is represented as a modal series.

In the reference plane $z = 0$ (see Figure 5), the fields can be written as a sum of orthonormal modes with the incident and reflected amplitudes at the discontinuity plane. In each waveguide (index $g=w$, for the larger, $g=s$ for the smaller), the following can be written:

$$\vec{\mathbf{E}}_t \Big|_{A_g, z=0} = \sum_{m=1}^{N_g} (a_m^{(g)} + b_m^{(g)}) \vec{\mathbf{e}}_m^{(g)}, \quad (4)$$

$$\vec{\mathbf{H}}_t \Big|_{A_g, z=0} = \sum_{m=1}^{N_g} (a_m^{(g)} - b_m^{(g)}) \vec{\mathbf{h}}_m^{(g)}$$

where $\vec{\mathbf{e}}_m^{(g)}, \vec{\mathbf{h}}_m^{(g)}$ are the transverse modal vectors corresponding to the m -th TE, TM, or TEM mode of the guide (g), which can be propagating or evanescent. These fields take the lateral boundary conditions into account while the electric and magnetic modal functions are related by the mode impedance as usual, which are also typically normalized to unity as follows.

$$\iint_{A_g} \vec{\mathbf{e}}_n^{(g)} \times \vec{\mathbf{h}}_m^{(g)} \cdot \hat{\mathbf{z}} dS = \begin{cases} 1, & m = n \\ 0, & m \neq n \end{cases}, \quad g \equiv w, s \quad (5)$$

The electric and magnetic field boundary conditions (EFBC and MFBC, respectively) for this problem relate the transversal fields in (4) at both sides of the discontinuity.

$$EFBC \text{ in } A_w: \widehat{\mathbf{z}} \times \vec{\mathbf{E}}^{(w)} = \begin{cases} 0 & \text{in } A_c, z = 0 \\ \widehat{\mathbf{z}} \times \vec{\mathbf{E}}^{(s)} & \text{in } A_s, z = 0 \end{cases} \quad (6)$$

$$MFBC \text{ in } A_s \text{ in: } \widehat{\mathbf{z}} \times \vec{\mathbf{H}}^{(w)} = \widehat{\mathbf{z}} \times \vec{\mathbf{H}}^{(s)} \quad \text{in } A_s, z = 0$$

These equations are imposed by means of a classic Galerkin method where the EFBC is tested by N_w magnetic modal fields $\vec{\mathbf{h}}_m^{(w)}$ from the larger waveguide, and the MFBC is tested with N_s electric modal fields $\vec{\mathbf{e}}_m^{(s)}$ in the smaller waveguide. This field-matching procedure also requires truncating the series (4) to N_g terms and collecting the modal amplitudes in column vectors. The final equations expressed in matrix form become

$$EFBC: (\mathbf{a}_w + \mathbf{b}_w) = \mathbf{X}^t (\mathbf{a}_s + \mathbf{b}_s), \quad (N_w \text{ eqs.}) \quad (7)$$

$$MFBC: \mathbf{X} (\mathbf{a}_w - \mathbf{b}_w) = (\mathbf{b}_s - \mathbf{a}_s), \quad (N_s \text{ eqs.}),$$

where matrix \mathbf{X} is filled with the interaction between the electric and magnetic modal functions from both waveguides in the step:

$$[X_{mn}] = \iint_{A_s} \vec{\mathbf{e}}_m^{(s)} \times \vec{\mathbf{h}}_n^{(w)} \cdot \widehat{\mathbf{z}} dS. \quad (8)$$

The equation system presented in (7) provides, after its resolution, the Generalized Scattering Matrix (GSM) \mathbf{S} of the problem in the form:

$$\begin{aligned} \mathbf{b} &= \mathbf{S}\mathbf{a}, \\ \mathbf{b}_w &= \mathbf{S}_{ww}\mathbf{a}_w + \mathbf{S}_{ws}\mathbf{a}_s \\ \mathbf{b}_s &= \mathbf{S}_{sw}\mathbf{a}_w + \mathbf{S}_{ss}\mathbf{a}_s \end{aligned} \quad (9)$$

with:

$$\begin{aligned} \mathbf{S}_{ww} &= \mathbf{X}^t \mathbf{F} \mathbf{X} - \mathbf{I}_w \\ \mathbf{S}_{ws} &= \mathbf{S}_{sw}^t = \mathbf{X}^t \mathbf{F} \\ \mathbf{S}_{ss} &= \mathbf{F} - \mathbf{I}_s \\ \mathbf{F} &= 2 (\mathbf{I}_s + \mathbf{X} \mathbf{X}^t)^{-1}. \end{aligned} \quad (10)$$

This formulation has been used in the past many times. Examples of the inner-cross product computation for different waveguide steps can be found in [25, 30, 31]. After this computation, the cascading of the GSM of each step in the problem is carried out systematically [14, 28], as it will be explained in the next section for the two proposed models.

4. Results for the Proposed Models

The mode-matching technique described in the previous section has been applied for the two proposed models in Figure 3, further detailed in this section. The first model uses two coaxial waveguides attached to both sides of a virtual circular waveguide filled by the sample material, which is

TABLE 1: Basic data for the test cases.

Item	Value
R_{outer} IO coaxial (b)	1.75 mm
R_{inner} IO coaxial (a)	0.46 mm
$\epsilon_{r,\text{coax}}$	2.54
$\epsilon_{r,\text{sample}}$ (MUT)	10-j0.1 ($\tan \delta_e = 0.01$)
$\mu_{r,\text{sample}}$ (MUT)	5-j0.05 ($\tan \delta_m = 0.01$)
Sample Thickness (d)	0.2 mm/1.0 mm
Frequency range	100 MHz – 20 GHz

denoted as *model A*. The second model takes into account the finite flanges used in the measurement, and it is called *model B*.

The test cases will be evaluated under the two models A and B, for the broadband frequency range from 0.1 GHz to 20 GHz, varying their constituent parameters. The coaxial waveguide used for the measurement has an inner and an outer radius of $a=0.46\text{mm}$ and $b=1.75\text{mm}$, respectively, filled by Teflon ($\epsilon'_{r,\text{coax}} = 2.5$) for providing 50Ω . The sample material for the tests has $\epsilon'_{r,\text{sample}} = 10$, $\epsilon''_{r,\text{sample}} = 0.1$ ($\tan \delta_e = 0.01$) and $\mu'_{r,\text{sample}} = 5$, $\mu''_{r,\text{sample}} = 0.05$ ($\tan \delta_m = 0.01$). This material is prepared with a thickness of $d=0.2\text{mm}$ and $d=1\text{mm}$. These main data are shown in Table 1.

The reference values are provided by the method from the *Dielectric Assessment Kit* (DAK) product line manufactured by the Swiss company SPEAG [32], used in high-precision systems for measurements of dielectric properties. These instruments allow dielectric parameter measurements over a very broad frequency range.

4.1. Model A with the Step between the Coaxial and the Large Circular Waveguide Containing the Sample. Model A is detailed in Figure 6. This model will be also divided into three cases (A1, A2, A3), depending on the boundary conditions used for the outer boundary of the virtual circular waveguide containing the sample. In all these cases, from the analysis point of view, the model only requires the characterization of two GSMs, called S^A and S^B according to Figure 6(b). However, S^A and S^B are only different in the port numbering, but both represent a step between the same types of waveguides with the same dimensions; the computational cost reduces to computing a single GSM, since once S^A is obtained, S^B is also available. Then, they have just to be cascaded through well-known operations to get the GSM representing the full structure.

4.1.1. Case Model A1: Large Virtual Circular Waveguide with PEW. Since the problem has no angular variation, under the TEM excitation by the coaxial line, the series (4) in the mode-matching will only require the TEM mode at the coaxial lines, and TM_{0n} modes at the coaxial and the circular waveguides. The field in the circular waveguide will be always represented in both models A and B by TM_{0n} modes. However, in order to see the importance of the higher-order TM_{0n} modes at the input/output, we will first compute in Figure 7 the

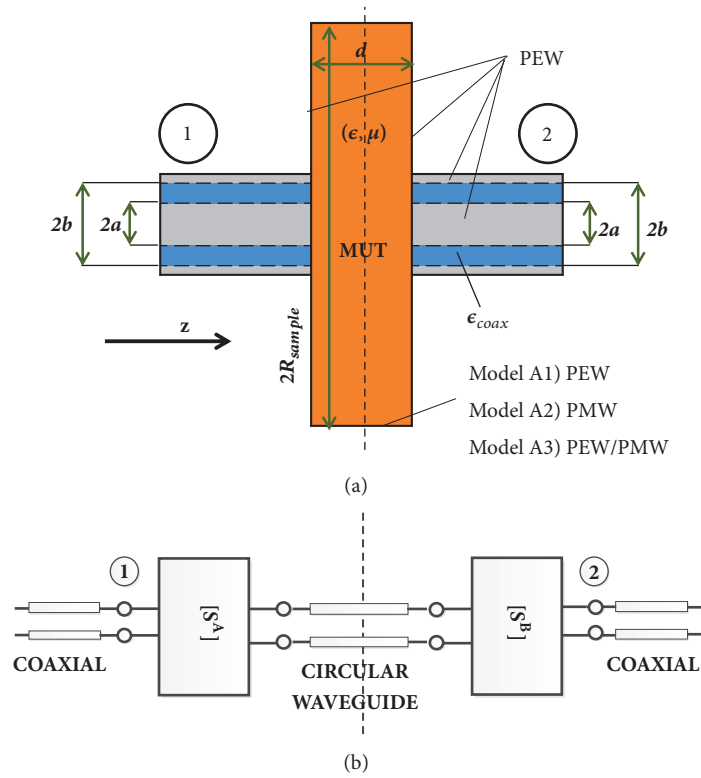


FIGURE 6: (a) Dimensions defining the model A (with revolution symmetry): case A1, PEW; case A2, PMW; case A3, combination of PEW and PMW; (b) Block diagram of the analysis by mode-matching, showing the symmetry plane.

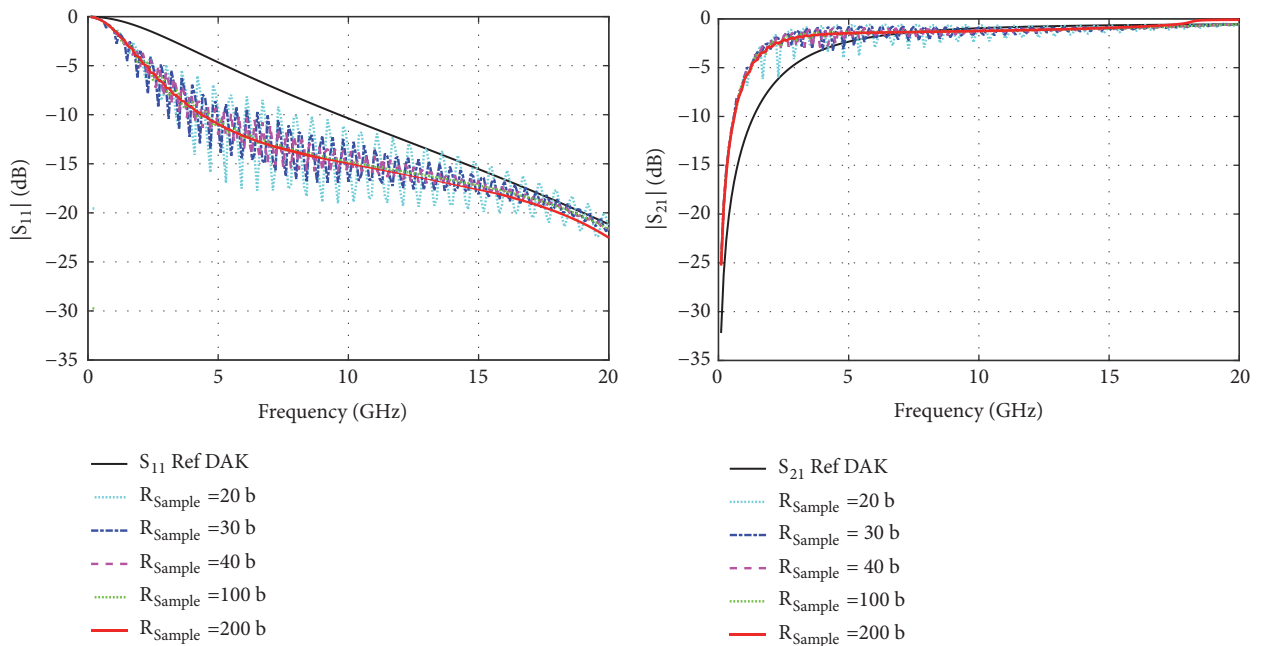


FIGURE 7: Magnitude (dB) of S_{11} and S_{21} for model A1 using only the TEM mode at the input/output coaxial lines, for different values of the virtual circular waveguide containing the sample (thickness $d=0.2$ mm).

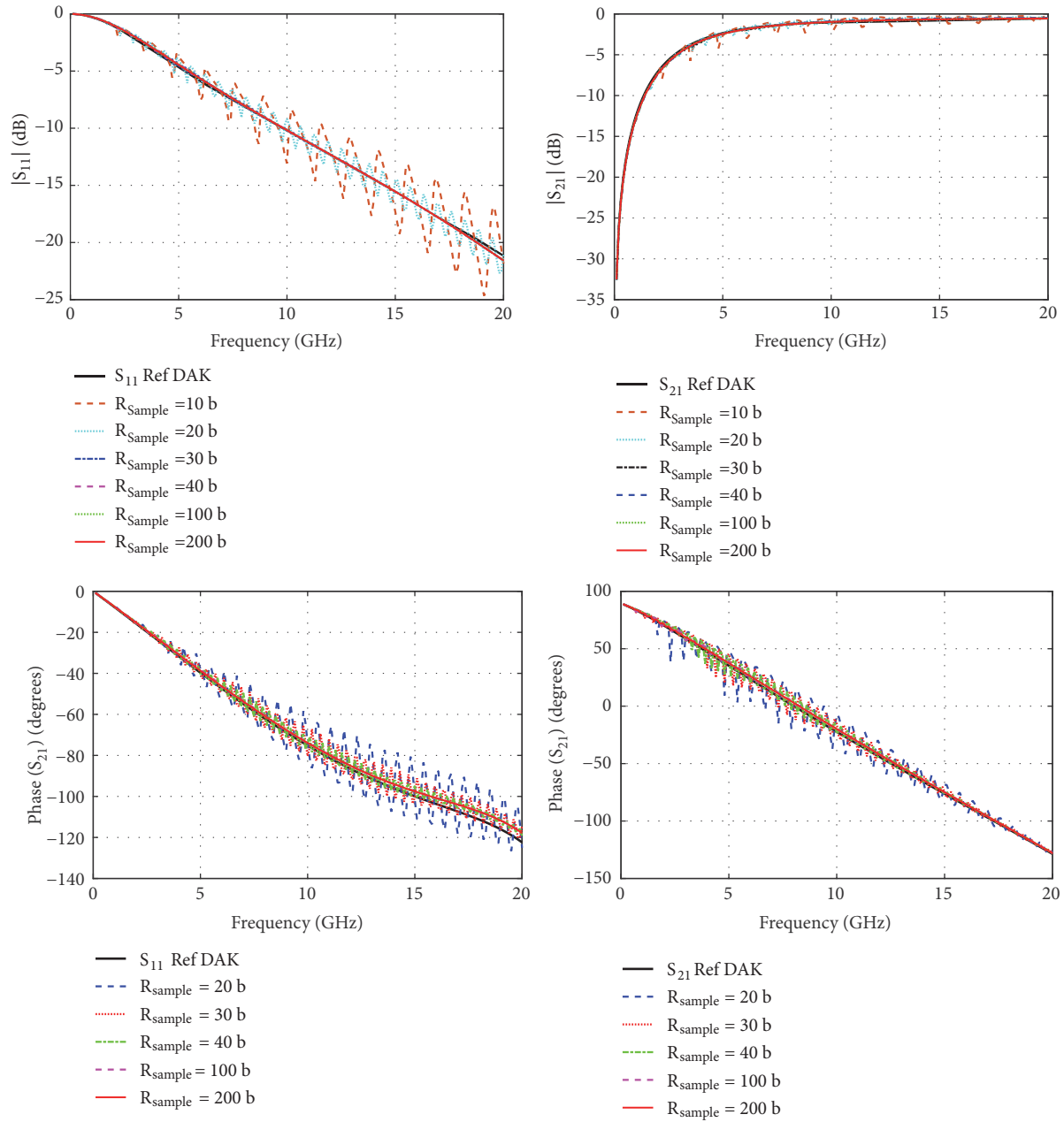


FIGURE 8: Magnitude (dB) and phase (degrees) of S_{11} and S_{21} for *model A1* with TEM and TM_{0n} modes at the input/output coaxial lines, for different values of the virtual circular waveguide containing the sample (thickness $d=0.2$ mm).

results by only using the TEM mode to approximate the field within the coaxial lines, as initial pioneer works with probes did.

In the simulation in Figure 7, the magnitude of the S_{11} and S_{21} parameters is shown for different values of the radius R_{sample} of the virtual circular waveguide between the input and output coaxial lines. The analysis starts with R_{sample} equal to 20 times the outer radius of the input/output coaxial, which shows a ripple that starts to decrease when this circular waveguide radius is enlarged. In this case, when R_{sample} increases, the results in both reflection and transmission are flatter and converge to the larger case of $R_{\text{sample}}=200b$.

However, the results do not reproduce the results of the DAK reference values, showing a relevant difference in the curves.

In order to overcome this issue, Figure 8 shows the same type of analysis as Figure 7, but using also TM_{0n} modes in the coaxial transmission lines in addition to the TEM mode. Although the ripple also appears as in the previous case and decreases when R_{sample} increases as well, now the results converge to those of the reference case obtained by DAK. Thus, the response improves the results obtained from the previous case, having a very good agreement. The phase is also shown in this graph, showing also a very good agreement. The phase reference is taken at the interface

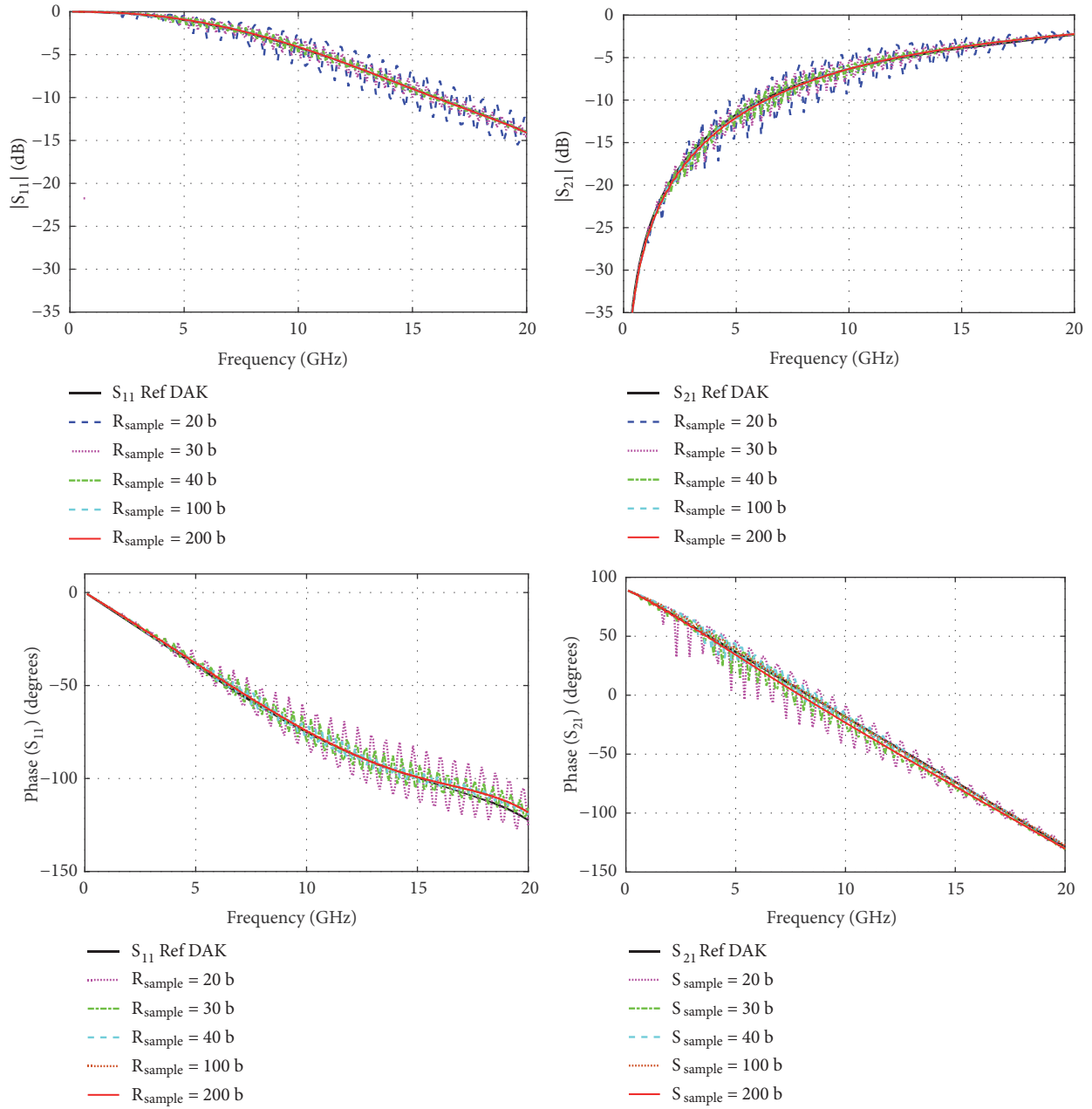


FIGURE 9: Magnitude (dB) and phase (degrees) of S_{11} and S_{21} for *model A1* with TEM and TM_{0n} modes at the input/output coaxial lines, for different values of the virtual circular waveguide containing the sample (thickness $d=1\text{mm}$).

between the coaxial and the circular waveguide in all the cases.

The same type of analysis is now done with the sample having a thickness of 1mm. From now on, the analysis will be always performed with TEM and TM_{0n} modes in the coaxial lines, since its need has been clearly justified in Figures 7 and 8. The results for the new thickness $d=1\text{mm}$ are shown in Figure 9, where the same type of performance as with the thinner sample can be seen: ripple in the curves related to the size of the large virtual circular waveguide containing the sample. This ripple reduces when the size of R_{sample} increases

till achieving convergent results matching those of the DAK reference.

4.1.2. Case Model A2: Large Virtual Circular Waveguide with PMW. In model A, we are expecting that the electromagnetic field at the lateral limit of the circular waveguide (i.e., for large ρ) is small enough to represent a suitable model for the actual measurement, where it is assumed that the field is confined within the MUT limits. In order to confirm that, the model should not provide very different results when the lateral

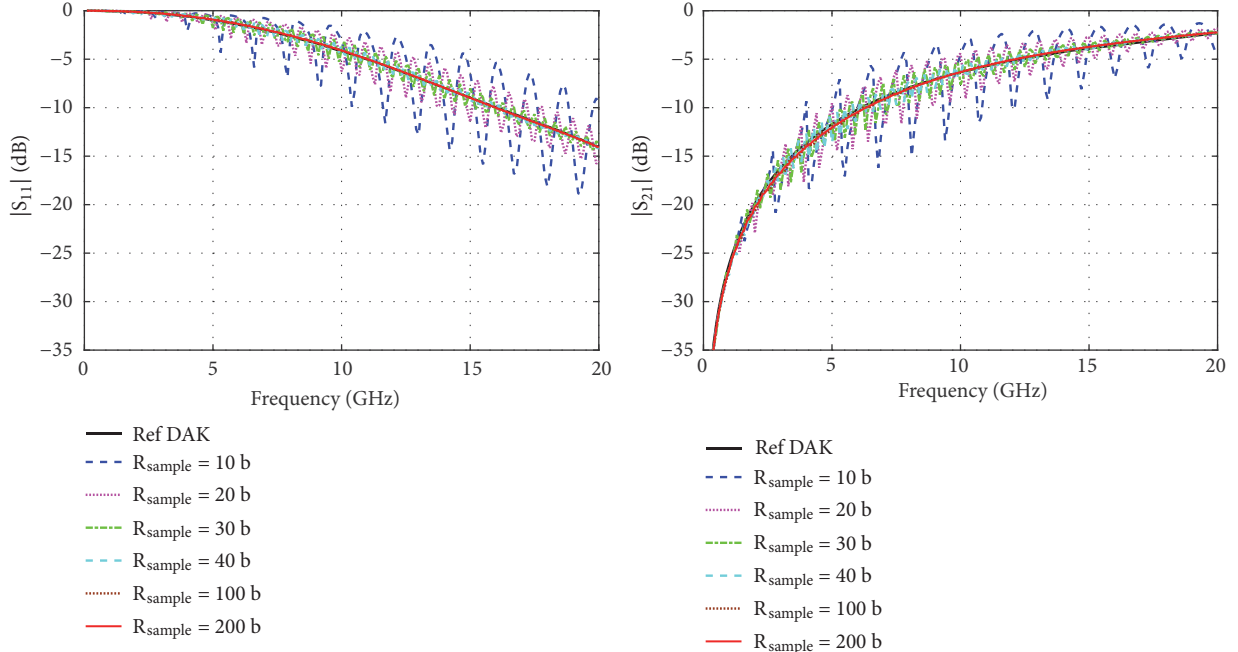


FIGURE 10: Magnitude (dB) of S_{11} and S_{21} for *model A2* with TEM and TM_{0n} modes at the input/output coaxial lines, for different values of the virtual circular waveguide containing the sample (thickness $d=1\text{mm}$).

boundary conditions of the circular waveguide are changed to PMW and the waveguide steps in Figure 6(b) are recomputed with these new modes. This is confirmed with the results shown in Figure 10 for a sample thickness of 1mm, where the magnitude of S_{11} and S_{21} has a very similar behavior to that of the case of model A1 with PEW in Figure 9. There is also a ripple in the mode-matching results, more important for smaller R_{sample} , which disappears when R_{sample} is large enough.

In all the simulations done so far, we have presented the results with a number of modes large enough to achieve convergent results with respect to the number of terms in the series (4). In this type of problems, as a general rule to overcome the relative convergence problem [14], the number of modes in the modal series is selected following a criterion related to the size of the involved waveguides. One possible solution is keeping a relation between the modes of the different waveguides as the square root of their areas. This means that for a step between circular waveguides, the ratio of the modes between two waveguides in a step discontinuity would be the ratio of their radii.

The convergence has been verified with several analyses, varying the number of modes while keeping a fixed geometry. One of those analyses is shown in Figure 11. It shows the results of this last case in Figure 10, although the behavior would be very similar for other geometries and for both models A or B. In Figure 11, the black solid line represents the reference and the other lines represent the results for different number of modes in the coaxial lines N_{coax} and in the large circular waveguide N_{circ} .

4.1.3. Case Model A3: Large Virtual Circular Waveguide with Combination of PEW and PMW. Figure 12 shows the results of models A1 and A2 with $R_{\text{sample}}=10b$ plotted within the same graph. It can be seen that the ripple of the responses for the two cases (PEW/PMW at the outer lateral boundary of the circular waveguide, respectively) are interleaved. This would also happen in the other results of Figures 9 and 10, although it is more difficult to see when the ripple starts to decrease for large R_{sample} . In addition, since both boundary conditions in the circular waveguide are approximations of the actual measurement problem, the combination of both results could be also another suitable analysis model. Moreover, this type of strategy has also been used in [26].

Following this rationale, Figure 12 also shows the combination of the PEW analysis in model A1 with those using the PMW in model A2, which will be the model A3 proposed in this subsection:

$$S_{11} = \frac{(S_{11}^{\text{PEW}} + S_{11}^{\text{PMW}})}{2}, \quad (11)$$

$$S_{21} = \frac{(S_{21}^{\text{PEW}} + S_{21}^{\text{PMW}})}{2}.$$

In order to verify model A3, Figure 13 shows the results for different values of R_{sample} . It can be seen how the combination of the two boundary conditions converges to the reference results with smaller R_{sample} , in both magnitude and phase. This translates into a higher computational efficiency, since a smaller number of modes will be needed to get the results using this smaller circular waveguide (in comparison with models A1, A2) containing the sample.

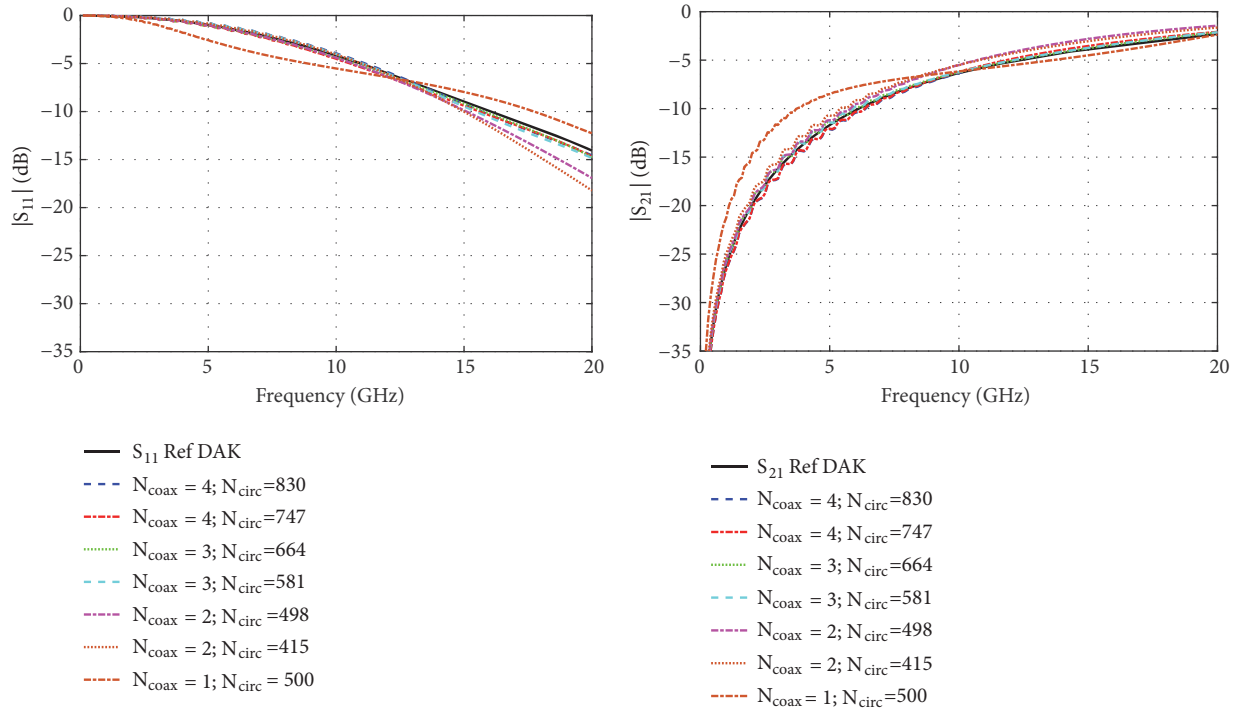


FIGURE 11: Convergence analysis. Magnitude (dB) of S_{11} and S_{21} for model A2 with TEM and TM_{0n} modes at the input/output coaxial lines, for different values of the number of modes N_{coax} and N_{circ} (thickness $d=1$ mm with $R_{\text{sample}}=200b$).

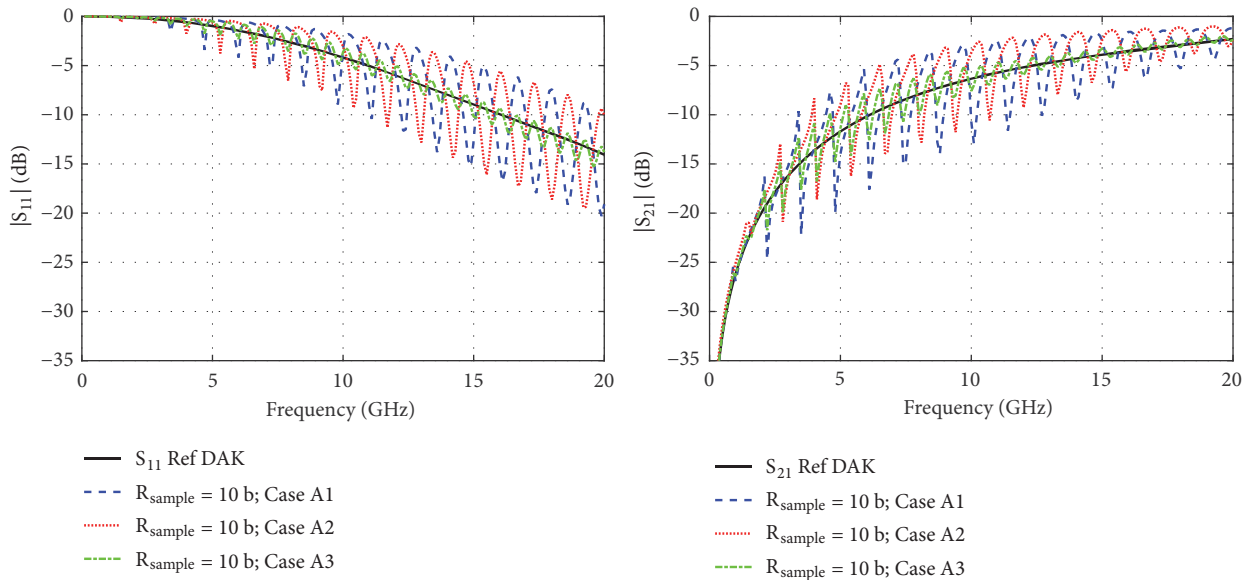


FIGURE 12: Magnitude (dB) of S_{11} and S_{21} comparing models A1, A2, and A3 with TEM and TM_{0n} modes at the input/output coaxial lines, for $R_{\text{sample}}=10b$ and sample thickness $d=1$ mm.

4.2. Model B with the Steps for Taking the Finite Flanges into Account. The second model to compute the two-port problem is shown in Figure 14. This geometry takes the finite flanges into account, as well as the outer size of the coaxial lines involved in the measurement. This may be relevant for some cases where the assumption that all

the fields are confined within the MUT limits starts to be not fully compliant with the experimental data. The structure has been plotted symmetrically with respect to the middle plane for the sake of the simplicity, but data from the input coaxial could be made different from the output coaxial.

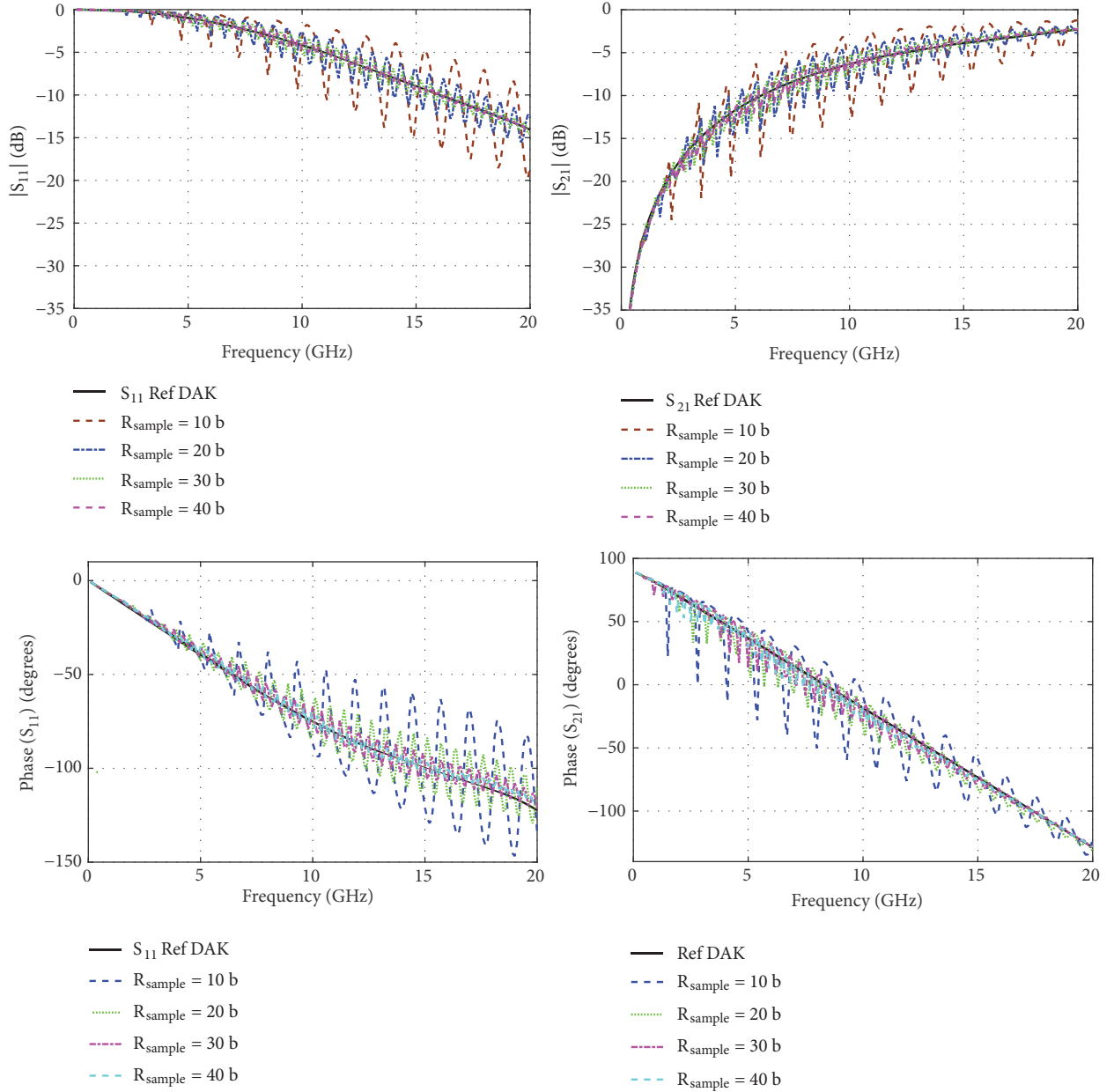


FIGURE 13: Magnitude (dB) and phase (degrees) of S_{11} and S_{21} for *model A3* with TEM and TM_{0n} modes at the input/output coaxial lines, for different values of the virtual circular waveguide containing the sample (thickness of $d=1\text{mm}$).

From the mode-matching point of view, the new geometry involves two new virtual coaxial transmission lines at each side of the problem, associated with the incorporation of the finite flange with radius R_{flange} and length L_{flange} to the model. They have an inner radius of R_o and R_{flange} , respectively, both with outer radius of R_{sample} . They are filled by air.

This geometry involves a new step discontinuity between the two virtual air-filled coaxial lines associated with the outer part of the structure, as is shown in Figure 14(b) with the block $[S_{coax}]$. Model B also involves a bifurcation between, at one side, the Teflon coaxial (radii a and b) and

one air-filled coaxial (radii R_{flange} and R_{sample}) and, at the other side, the larger circular waveguide of radius R_{sample} . In this problem, two additional virtual ports appear, carrying the signal not confined within the MUT limits and not taken into account by model A. Once the GSM of the steps and bifurcations are computed, they are also easily cascaded.

For the following tests, in addition to the data in Table 1, the flange length will be $L_{flange}=1\text{mm}$, with a cover for the input/output coaxial of 0.5mm thickness, i.e., $R_o=b+0.5\text{mm}$. As was done for model A, the first simulation in Figure 15 is done using a fixed geometry

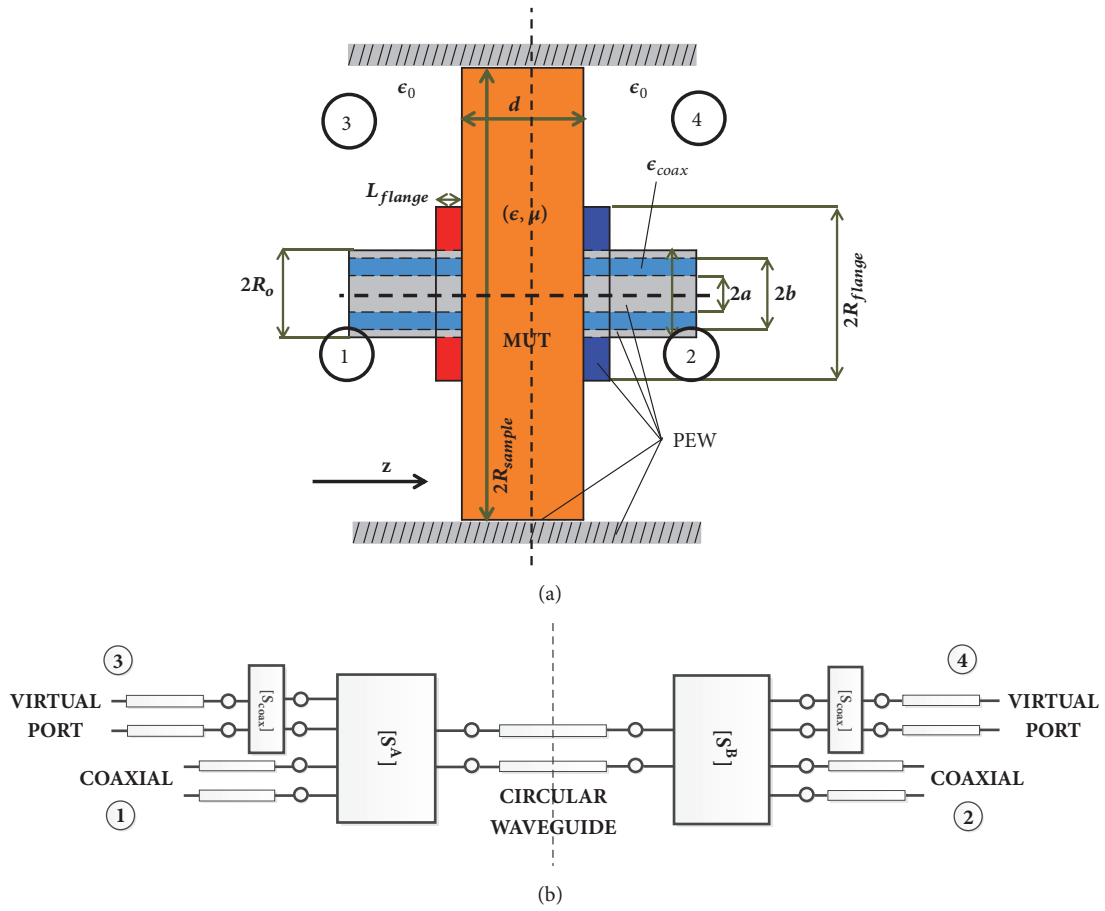


FIGURE 14: (a) Dimensions defining the model B (with revolution symmetry) taking the finite flanges into account. (b) Block diagram of the analysis by mode-matching, showing the symmetry plane.

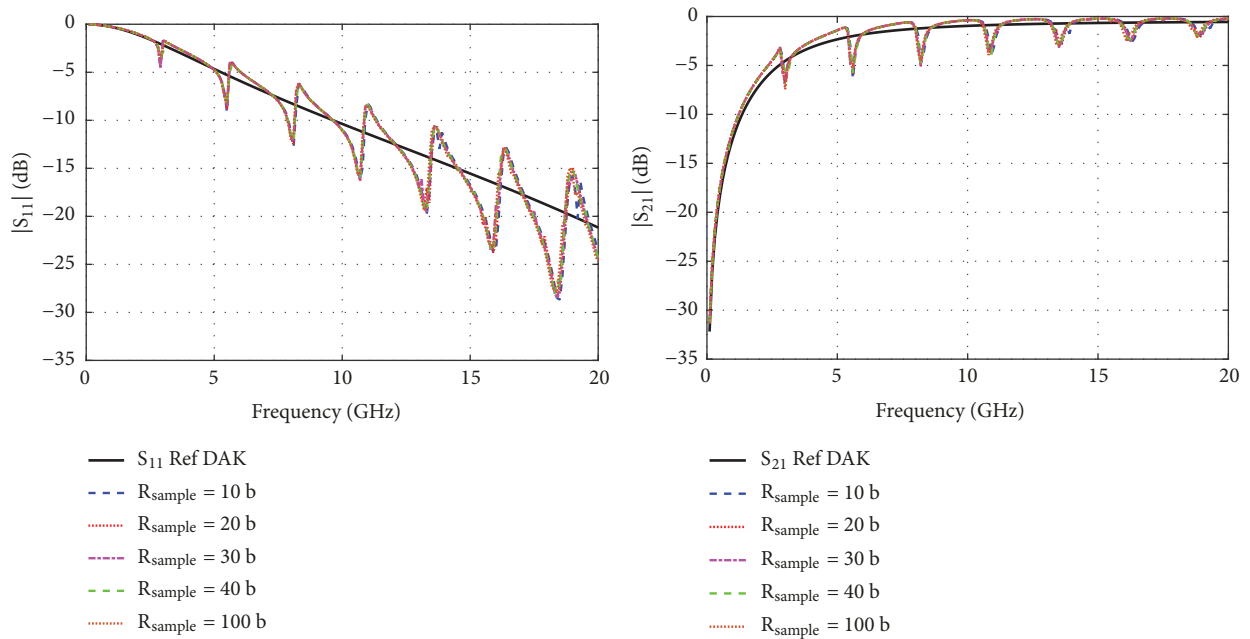


FIGURE 15: Magnitude (dB) of S_{11} and S_{21} for model B with TEM and TM_{0n} modes at the input/output coaxial lines, for different values of the R_{sample} (thickness $d=0.2$ mm, $R_{flange}=5.4b$).

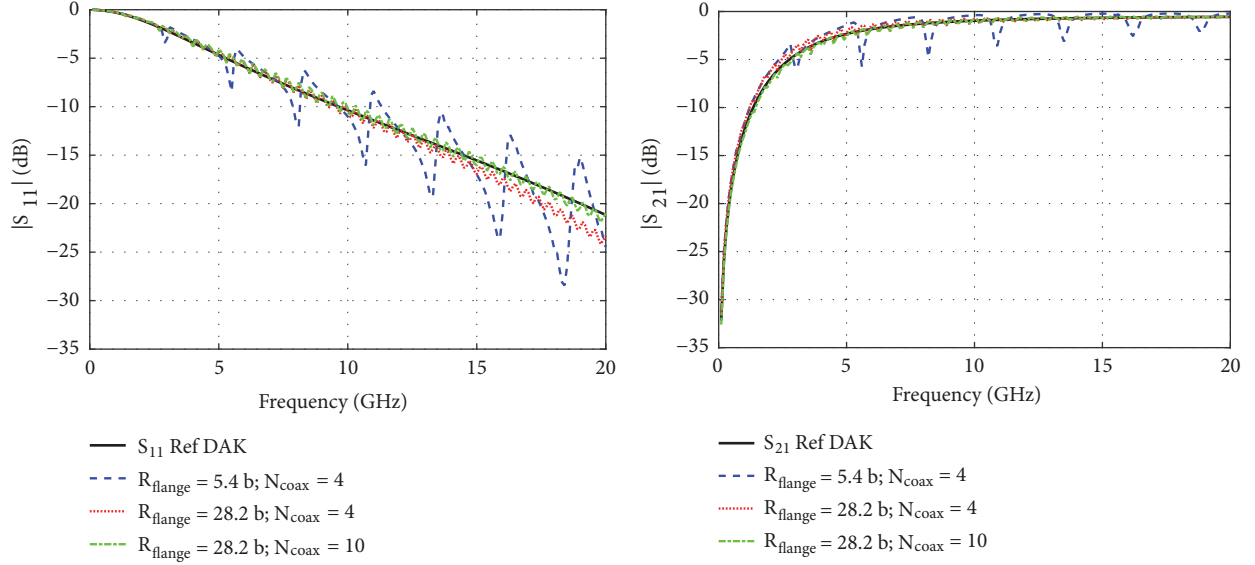


FIGURE 16: Magnitude (dB) of S_{11} and S_{21} for *model B* with TEM and TM_{0n} modes at the input/output coaxial lines, for different values of the flange size, and number of modes (thickness $d=0.2$ mm, $R_{sample}=50b$).

with finite $R_{flange} = 5.4b$, varying the radius of the R_{sample} associated with the circular waveguide between $10b$ and $100b$. In this case, although the results are very similar for the different R_{sample} , the finite size of the flange is leading to results different from those of the DAK reference, regardless of the size of the virtual circular waveguide required in the mode-matching simulations. The DAK values corresponded to the typical geometry with a large enough flange and electromagnetic field fully confined within the MUT limits, which is coherent with results of model A.

This effect of the size of the flange is further analyzed in Figure 16, where the simulations are run with different number of modes and different values for R_{flange} . The ripple is now associated with R_{flange} since these simulations have a fixed value of R_{sample} . It is also important to note that additional terms in series (4) are needed for having convergent results in terms of number of modes, since now the structure is more complex involving more waveguide steps.

In this case, since the new air-filled coaxial lines have a large size, many modes will be needed to approximate the field within them, with a high aspect ratio between the outer and inner conductor. Thus, their modes will have to be computed carefully to avoid instabilities related to the behavior of the $Y_n(u)$ function in (3) when it is evaluated close to zero.

Figure 17 shows the results of model B for different values of R_{flange} in Figure 14(a), with a fixed value of R_{sample} . Results show that for a large flange, the DAK reference is achieved. Figure 17 also shows the backward and forward radiation for different values of the flange, characterized

by the S-parameter between the input (or output) Teflon coaxial port and the virtual air-filled coaxial ports 3 and 4 in Figure 14. As expected, for a smaller flange, large peaks of signal at specific frequencies are not confined within the MUT limits. Figure 18 shows the same type of analysis of Figure 17 for a thickness of 1mm, where it can be seen that these peaks of forward and backward radiation are less significant.

5. Conclusions

The mathematical formulation of the mode-matching method applied to the two-port scattering problem arising in a material placed between two coaxial probes has been presented. This well-known configuration has received renewed attention in very recent years. In this line, this paper has developed two different approaches to characterize this dielectric measurement setup for broadband applications. The analysis of the problem with the MUT considering both PMW and PEW has been studied, while their combination has been shown to improve the efficiency of the method. In all cases, the use of higher-order modes in the coaxial waveguide at the MUT interface is essential to obtain fast and accurate results. The effect of the finite flanges has been also efficiently and rigorously assessed, proving that a flatter frequency response is achieved when the field is confined within the MUT, i.e., when large flanges are considered. Two setups have been analyzed and their results have been compared with the reference data provided by the DAK characterization method, showing excellent agreement between them.

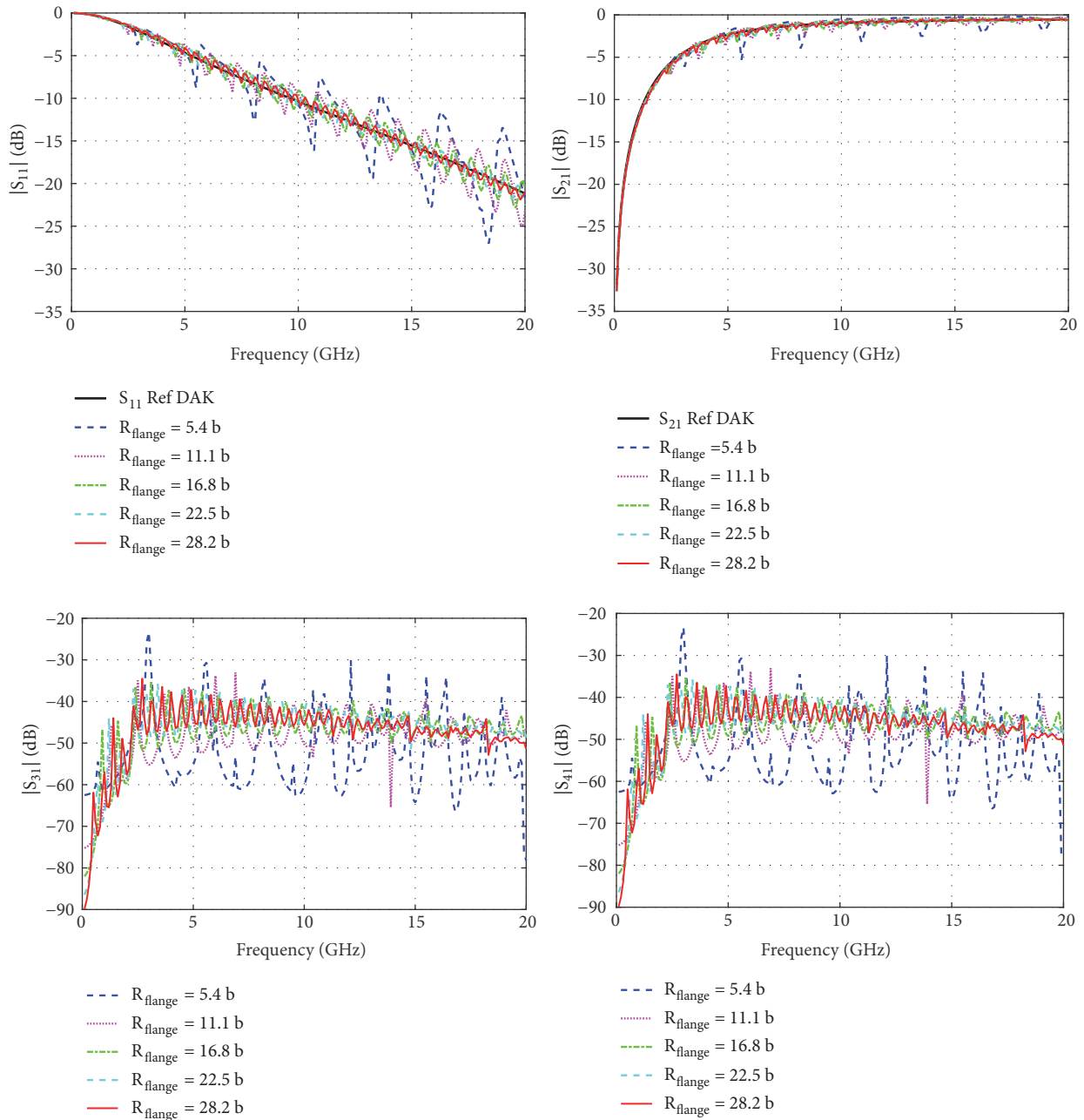


FIGURE 17: Magnitude (dB) of S_{31} and S_{41} for *model B* with TEM and TM_{0n} modes at the input/output coaxial lines, for different values of the flange size (thickness $d=0.2$ mm, $R_{sample}=50b$).

Data Availability

The data used to support the findings of this study are available from the corresponding author upon request.

Conflicts of Interest

The authors declare that there are no conflicts of interest regarding the publication of this paper.

Acknowledgments

This work was supported in part by the Spanish Government (Agencia Estatal de Investigación, Fondo Europeo de Desarrollo Regional) under Grant TEC2016-76070-C3-1/2-R (AEI/FEDER, UE) and in part by the program of Comunidad de Madrid under Grant S2013/ICE-3000. The authors want to acknowledge SPEAG company, Zurich, Switzerland, especially Pedro Crespo-Valero and Ferenc Muranyi, for their assistance with the DAK results.

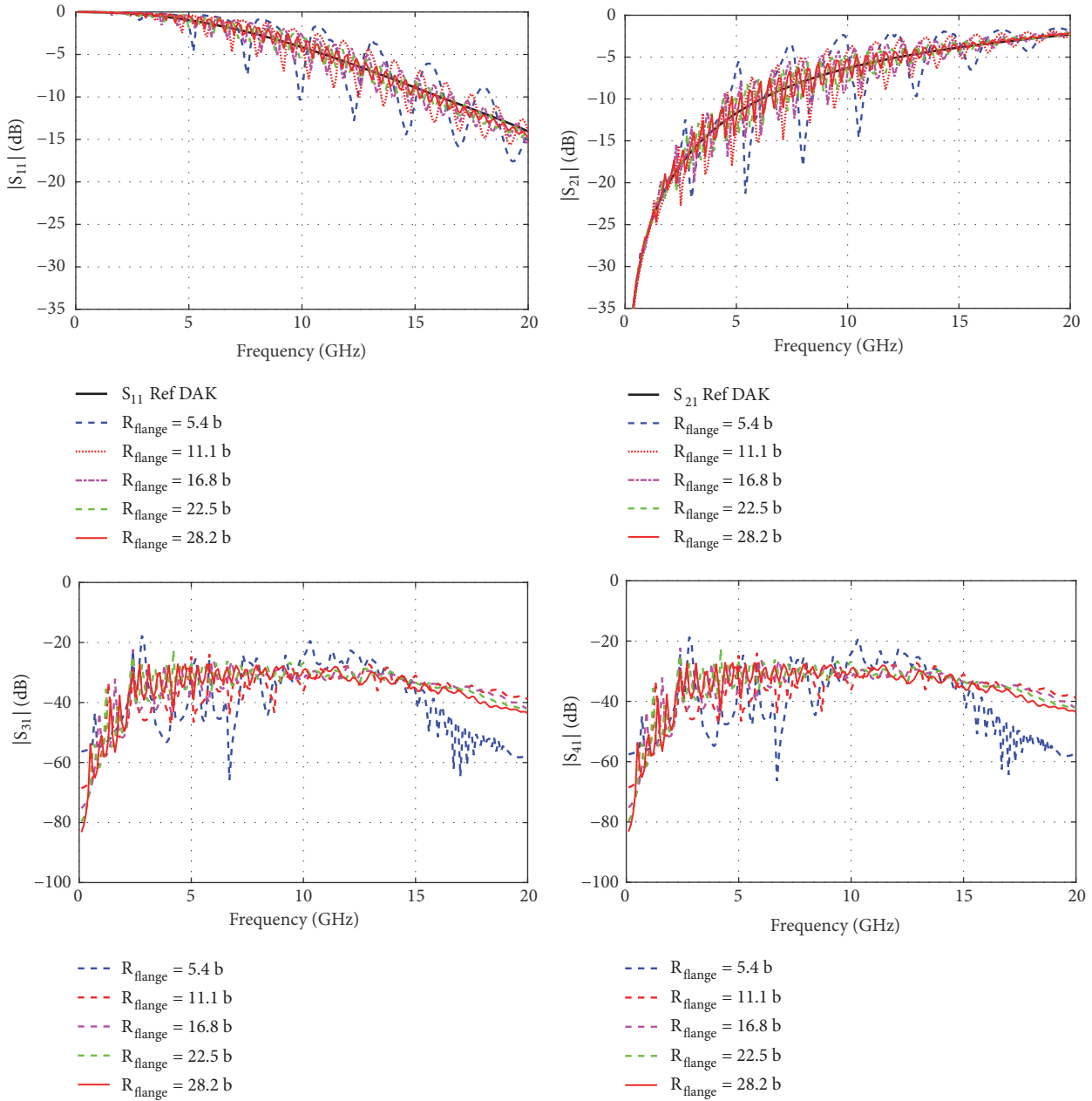


FIGURE 18: Magnitude (dB) of S_{31} and S_{41} for model B with TEM and TM_{0n} modes at the input/output coaxial lines, for different values of the flange size (thickness $d=1$ mm, $R_{\text{sample}}=50b$).

References

- [1] Keysight Technologies, “Basics of measuring the dielectric properties of materials,” Application Note 5989-2589EN, USA, March 7, 2017.
- [2] V. Komarov, S. Wang, and J. Tang, “Permittivity and measurement,” in *Encyclopedia of RF and Microwave Engineering*, pp. 1–20, John Wiley & Sons, 2005.
- [3] U. Kaatzte and Y. Feldman, “Broadband dielectric spectrometry of liquids and biosystems,” *Measurement Science and Technology*, vol. 17, no. 2, pp. R17–R35, 2006.
- [4] A. P. Gregory and R. N. Clarke, “A review of RF and microwave techniques for dielectric measurements on polar liquids,” *IEEE Transactions on Dielectrics and Electrical Insulation*, vol. 13, no. 4, pp. 727–743, 2006.
- [5] R. W. Bruce, “New Frontiers in the Use of Microwave Energy: Power and Metrology,” in *Proceedings of the Materials Research Society Symposium*, vol. 124, pp. 3–15, 1990.
- [6] L. F. Chen, C. K. Ong, C. P. Neo, V. V. Varadan, and V. K. Varadan, *Microwave Electronics: Measurement and Materials Characterization*, John Wiley & Sons, Ltd, 2004.
- [7] D. M. Pozar, *Microwave Engineering*, John Wiley, Hoboken, NJ, USA, 2011.
- [8] R. W. P. King and L. D. Scott, “The Cylindrical Antenna as a Probe for Studying the Electrical Properties of Media,” *IEEE*

- Transactions on Antennas and Propagation*, vol. 19, no. 3, pp. 406–416, 1971.
- [9] E. C. Burdette, F. L. Cain, and J. Seals, “In vivo probe measurement technique for determining dielectric properties at VHF through microwave frequencies,” *IEEE Transactions on Microwave Theory and Techniques*, vol. 28, no. 4, pp. 414–427, 1980.
- [10] J. R. Mosig, J.-C. E. Besson, M. Gex-Fabry, and F. E. Gardiol, “Reflection of an open-ended coaxial line and application to nondestructive measurement of materials,” *IEEE Transactions on Instrumentation and Measurement*, vol. IM-30, no. 1, pp. 46–51, 1981.
- [11] J. D. Baños-Polglase and J. D. Rebollar, “Coaxial probes with finite ground plane,” *IEEE Electronics Letters*, vol. 24, no. 5, pp. 291–292, 1988.
- [12] P. J. B. Clarricoats and K. R. Slinn, “Numerical method for the solution of waveguide-discontinuity problems,” *IEEE Electronics Letters*, vol. 2, no. 6, pp. 226–228, 1966.
- [13] A. Wexler, “Solution of waveguide discontinuities by modal analysis,” *IEEE Transactions on Microwave Theory and Techniques*, vol. 15, no. 9, pp. 508–517, 1967.
- [14] T. Itoh, *Numerical Techniques for Microwave and Millimeter-Wave Passive Structures*, John Wiley, New York, NY, USA, 1989.
- [15] M. W. Hyde and M. J. Havrilla, “A broadband, nondestructive microwave sensor for characterizing magnetic sheet materials,” *IEEE Sensors Journal*, vol. 16, no. 12, pp. 4740–4748, 2016.
- [16] M. W. Hyde, M. J. Havrilla, and A. E. Bogle, “Nondestructive determination of the permittivity tensor of a uniaxial material using a two-port clamped coaxial probe,” *IEEE Transactions on Microwave Theory and Techniques*, vol. 64, no. 1, pp. 239–246, 2016.
- [17] M. H. Hosseini, H. Heidar, and M. H. Shams, “Wideband nondestructive measurement of complex permittivity and permeability using coupled coaxial probes,” *IEEE Transactions on Instrumentation and Measurement*, vol. 66, no. 1, pp. 148–157, 2017.
- [18] D. K. Misra and M. Chhabra, “A quasi-static analysis of open-ended coaxial lines,” *IEEE Transactions on Microwave Theory and Techniques*, vol. 35, no. 10, pp. 925–928, 1987.
- [19] J. Baker-Jarvis, M. Janezic, P. Domich, and R. Geyer, “Analysis of an open-ended coaxial probe with lift-off for nondestructive testing,” *IEEE Transactions on Instrumentation and Measurement*, vol. 43, no. 5, pp. 711–718, 1994.
- [20] D. V. Blackham and R. D. Pollard, “An improved technique for permittivity measurements using a coaxial probe,” *IEEE Transactions on Instrumentation and Measurement*, vol. 46, no. 5, pp. 1093–1099, 1997.
- [21] B. García-Baños, J. M. Catalá-Civera, A. J. Canós, and F. Peñaranda-Foix, “Design rules for the optimization of the sensitivity of open-ended coaxial microwave sensors for monitoring changes in dielectric materials,” *Measurement Science and Technology*, vol. 16, no. 5, pp. 1186–1192, 2005.
- [22] R. A. Weck, “Thin-Film Shielding for Microcircuit Applications and a Useful Laboratory Tool for Plane-Wave Shielding Evaluations,” *IEEE Transactions on Electromagnetic Compatibility*, vol. 10, no. 1, pp. 105–112, 1968.
- [23] A. R. Ondrejka and J. W. Adams, “Shielding effectiveness (SE) measurement techniques,” in *Proceedings of the IEEE National Symposium on Electromagnetic Compatibility*, pp. 1–6, 1984.
- [24] J. Baker-Jarvis and M. D. Janezic, “Analysis of a two-port flanged coaxial holder for shielding effectiveness and dielectric measurements of thin films and thin materials,” *IEEE Transactions on Electromagnetic Compatibility*, vol. 38, no. 1, pp. 67–70, 1996.
- [25] A. P. Orfanidis, G. A. Kyriacou, and J. N. Sahalos, “A mode-matching technique for the study of circular and coaxial waveguide discontinuities based on closed-form coupling integrals,” *IEEE Transactions on Microwave Theory and Techniques*, vol. 48, no. 5, pp. 880–883, 2000.
- [26] Z. Shen and R. H. MacPhie, “Input admittance of a multilayer insulated monopole Antenna,” *IEEE Transactions on Antennas and Propagation*, vol. 46, no. 11, pp. 1679–1686, 1998.
- [27] L. Polo-Lopez, J. A. Ruiz-Cruz, J. R. Montejo-Garai, and J. M. Rebollar, “Analysis of waveguide discontinuities with lateral and transverse perfect magnetic wall boundary conditions,” in *Proceedings of the 2016 URSI International Symposium on Electromagnetic Theory, EMTS 2016*, pp. 811–814, Finland, August 2016.
- [28] J. M. Rebollar and J. A. Encinar, “Field theory analysis of multiport-multidiscontinuity structures: application to short-circuited E-plane septum,” *IEE Proceedings Part H: Microwaves, Antennas and Propagation*, vol. 135, no. 1, pp. 1–7, 1988.
- [29] R. E. Collin, *Field Theory of Guided Waves*, IEEE Press, New York, NY, USA, 1991.
- [30] Z. Shen and R. H. MacPhie, “Scattering by a Thick Off-Centered Circular Iris in Circular Waveguide,” *IEEE Transactions on Microwave Theory and Techniques*, vol. 43, no. 11, pp. 2639–2642, 1995.
- [31] A. Morán-López, J. Córcoles, J. A. Ruiz-Cruz, J. R. Montejo-Garai, and J. M. Rebollar, “Electromagnetic Scattering at the Waveguide Step between Equilateral Triangular Waveguides,” *Advances in Mathematical Physics*, vol. 2016, Article ID 2974675, pp. 1–16, 2016.
- [32] DAK, “DAK - Dielectric Assessment Kit Product Line,” <https://spag.swiss/products/dak/dielectric-measurements>.



Hindawi

Submit your manuscripts at
www.hindawi.com

